

**GT2011-46700**

## **EXPERIMENTAL INVESTIGATION OF DISC CAVITY LEAKAGE FLOW AND HUB ENDWALL CONTOURING IN A LINEAR ROTOR CASCADE**

**Ryan D. Erickson<sup>†</sup> and Terrence W. Simon**

Department of Mechanical Engineering  
University of Minnesota  
Minneapolis, Minnesota, U.S.A

**Luzeng Zhang and Hee-Koo Moon**

Solar Turbines Incorporated  
San Diego, California, U.S.A.

### **ABSTRACT**

An experimental study is carried out in a stationary linear cascade which simulates a turbine rotor to compare the thermal performance of two new axisymmetric endwall contour geometries. Measurements of endwall adiabatic film cooling effectiveness and near-endwall passage temperature fields are made for this purpose. In addition to documenting endwall contouring effects, a range of disc cavity leakage flow rates is investigated. This information is meant to quantify, over the range tested, the benefits and penalties of introducing leakage flow into the passage using the designated endwall contouring. Special attention is paid to determine whether the endwall curvature has any effect on the interaction between mainstream and secondary flows within the passage. Results indicate improved thermal performance when strong endwall curvature exists near the blade leading edge. The strong curvature causes cavity leakage flow to remain closer to the endwall, thereby increasing cooling effectiveness.

Keywords: endwall, rotor, platform, contouring, leakage flow

### **INTRODUCTION**

Hot gas path aerodynamics and heat transfer continue to receive attention by designers and researchers with the motivation of driving turbine inlet temperatures higher to increase thermal efficiency and specific power. The need to provide ample thermal protection for engine components while most effectively using cooling resources is central to this study. One area which is susceptible to damage from high turbine entry temperatures is the cavity between the stator and rotor disc. This cavity exists in order to provide clearance between stationary and moving components. The cavity dimensions can vary as a result of transient operating conditions, but the ideal

cavity is as small as practical. In order to prevent hot gas from flowing into this space, leakage (or purge) flow is delivered to the area and ejected into the gas path. Current designs meter flow bled from the high pressure compressor into the cavity using labyrinth seals. This flow, used to prevent ingestion of hot gas from the passage, also offers cooling potential within the rotor passage. This disc cavity leakage flow was shown to have an effect on endwall secondary flows. A study by Maclean et al. [1] demonstrated that leakage flow can increase secondary losses. This is largely due to entrainment of leakage flow within the passage vortex as detailed in several studies from the von Kármán Institute (e.g. Dénos et al. [2], Paniagua et al. [3], and Pau et al. [4]). Other disc cavity designs have been studied which allow for leakage flow ejection which is not entirely radial. One, by Ong et al. [5], incorporates a small downward step between the stator rim and a rounded rotor platform. They found that leakage flow enters the passage with less swirl than that of the main flow, effectively decreasing efficiency in downstream blade rows due to enhanced mixing by stronger secondary flows. They also cite the velocity difference of leakage and mainstream flows as a source of loss at the injection location due to mixing, and note an improvement in stage efficiency when injecting leakage flow is introduced with additional swirl. A similar computational study by Marini and Girgis [6] looks at the effects of modifying the endwall leading edge shape on mainstream/leakage flow interaction. They compared one endwall contour that was recessed below the stator rim with one that was level with the rim. Results suggest that the recessed endwall design is more sensitive to changes in leakage flow rates and produces lower stage efficiency than that computed with the no-step counterpart.

Interestingly, upstream air injection has also been used to modify the formation of secondary flows. Researchers such as

<sup>†</sup>Present address, 3M Center, Building 235-03-F-08  
St. Paul, MN 55144-100

Blair [7], Biesinger and Gregory-Smith [8], and others, have shown that injecting air upstream through slots and holes can, in some cases, influence secondary flow formation (sometimes such evidence is deduced from heat transfer measurements). Their geometries, used for air injection experiments to test for the control of secondary flows were predominantly slots, instead of disc cavities. Nevertheless, their findings are relevant. Under certain conditions, various researchers (see Simon and Piggush [9]) were able to decrease the effects of secondary flows on losses and heat transfer. Special consideration in these cases was given to injected air-to-mainstream pressure ratios, mass flow rates, and injection angle. Thus, in the case of disc cavity leakage flow, the injection geometry becomes very important as it helps dictate the mixing interaction between hot gas path flow and leakage flow which exits the disc cavity.

The current study implements a disc cavity geometry with no step between the stator and rotor endwalls. The rotor hub endwall is contoured in its upstream portion to control the way in which leakage flow is mixed with the passage flow. The cooling potential of disc cavity leakage flow is measured to identify any benefits endwall contouring may provide in this area. A companion study by Erickson and Simon [10] provides aerodynamic loss data for these endwall contours.

Though the present study is of a first stage rotor, the facility is a single-row, stationary cascade. It captures many dominate effects in the flow of this stage, such as mixing of leakage and passage flows and secondary flows in the passage. Missing from the experiment are the passing wakes from upstream airfoils, the relative movement of the endwalls with the associated skewing of the endwall boundary layer flow, and the effects of rotation on the flow passing through the leakage path and within the rotor passage. Experiments with all of these effects added to the cases studied herein are very complex and do not offer much opportunity to evaluate effects separately. Nevertheless, they represent valuable extensions beyond the present work. One study that exemplifies rotation is by Suryanarayanan et al. [11].

## NOMENCLATURE

$C$	Blade Chord Length [m]
$C_{ax}$	Axial Chord Length [m]
$C_p$	Coefficient of Pressure [dimensionless]
$Lu$	Turbulence Energy Length Scale [m]
$MFR$	Leakage-to-Mainstream Mass Flow Ratio [%]
$P_s$	Static Pressure [Pa]
$P_t$	Total Pressure [Pa]
$Re_c$	Reynolds Number scaled on Blade Chord Length
$S$	Blade Span [m]
$Tu$	Turbulence Intensity [%]
$U_0$	Approach Flow Velocity [m/s]
$x$	Passage Axial Coordinate [m]
$y$	Passage Pitchwise Coordinate [m]
$z$	Passage Spanwise (Endwall-Normal) Coordinate [m]

## Greek

$\varepsilon$	Turbulence Dissipation [ $m^2/s^3$ ]
$\eta$	Adiabatic Effectiveness Value [dimensionless]
$\theta$	Recovery Temperature [dimensionless]
$\Lambda$	Turbulence Integral Length Scale [m]
$\rho$	Density [ $kg/m^3$ ]

## Subscripts

0	Located at Passage Inlet Plane
1	Located at Passage Exit Plane
$\ell$	Located at Leakage Flow Rim Seal Slot
$w$	Wall Property

## EXPERIMENTAL FACILITY AND FLOW CONDITIONS

The test section is designed to simulate the geometry and flow inside an airfoil passage of a modern, mid-sized gas turbine engine. It is a two passage cascade which contains three rotor blades, a contoured hub endwall (two designs were considered), a flat endwall, a disc cavity leakage flow slot and plenum, and an approach flow temperature contouring slot for creation of a thermal boundary layer.

The cascade layout is shown in Fig. 1 with corresponding dimensions given in Table 1. The rotor blade profile is obtained from a cross-section of a three-dimensional blade in a mid-sized modern industrial gas turbine. A scaling factor of approximately 14x is used for these blades in reference to their size in the actual engine. Each blade is constructed with 40 static pressure taps around the perimeter at midspan ( $S = 0.5$ ). Boundary layer bleed slots are incorporated into the wind tunnel walls to align the stagnation points at the leading edges of the upper and lower blades. Additionally, tailboards are adjusted at the cascade exit to create periodic boundary conditions within the blade passages. Though the geometry is that of a rotor section, the entire facility is stationary.

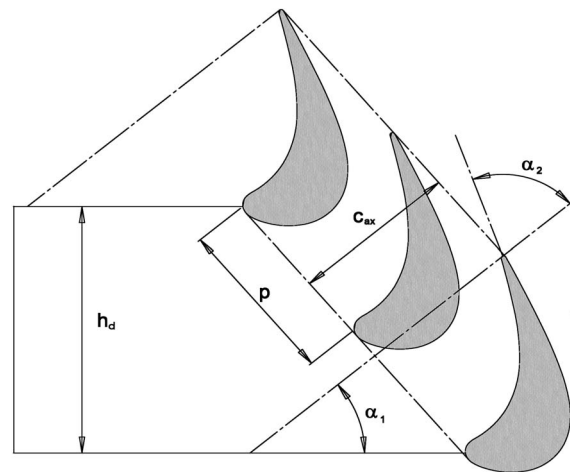
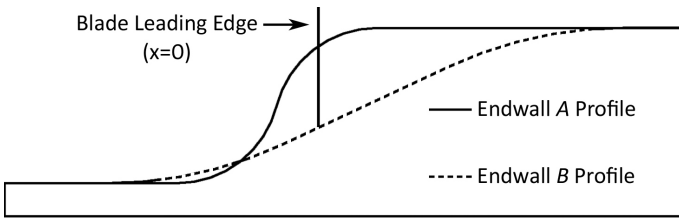


Figure 1. Cascade Layout

**Table 1. Cascade Dimensions**

Scale Factor:	14.06
Chord Length ( $c$ ):	55.79 cm
Axial Chord ( $c_{ax}$ ):	43.20 cm
Pitch ( $p$ ):	42.10 cm
Blade Aspect Ratio:	1.20
Inlet Flow Angle ( $\alpha_1$ ):	40.0°
Outlet Flow Angle ( $\alpha_2$ ):	70.0°
Inlet Duct Height ( $h_d$ ):	64.50 cm
Inlet Duct Width ( $w_d$ ):	50.60 cm

The two hub endwall designs are constructed as interchangeable components for use in the cascade facility. The designs will be referred to as endwalls “A” and “B” and are depicted in Fig. 2 relative to the blade leading edge plane ( $x = 0$ ). Both designs are contoured in the axial direction and share a common downstream elevation. This elevation is also common to the wind tunnel approach flow wall. Thus, no upward or downward step exists between the approach flow wall and hub endwall. This can be seen in Fig. 3. Endwall contour *A* displays very strong curvature beginning at  $x/C_{ax} = -0.14$ . This concave section meets tangent to a convex curve extending to  $x/C_{ax} = 0.06$ , just past the blade’s leading edge. In contrast, endwall contour *B* is much more gradual, beginning at  $x/C_{ax} = -0.21$  and extending further inside the passage at  $x/C_{ax} = 0.31$ .

**Figure 2. Axial Contours for Endwalls A and B**

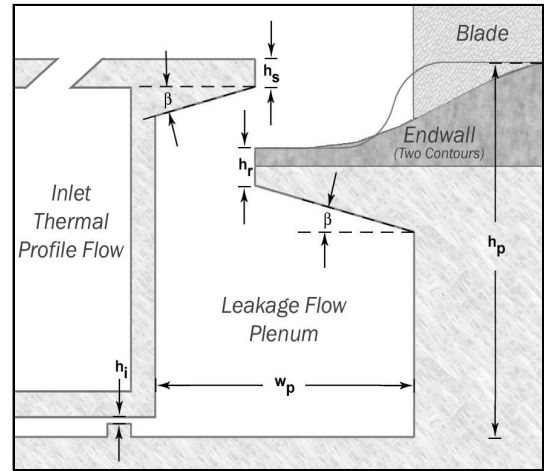
Disc cavity leakage (purge) flow is introduced into the rotor passage by means of a leakage flow plenum and slot, as shown in Fig. 3. The plenum is designed to simulate the disc cavity components through which leakage air flows in a real engine. Dimensions scaled from a modern gas turbine engine drawing are reported in Table 2. The leakage flow is delivered into the channel in the bottom left corner of Fig. 3. As it travels through the channel, it is abruptly met with a contraction designed to simulate a rim (labyrinth) seal in the engine. Past the rim seal, the leakage flow enters into a large open volume where it mixes and is directed upward. It then travels through the leakage flow slot and onto the contoured hub endwall.

Of particular importance to this study is the amount of flow entering the leakage plenum. This leakage flow rate is scaled on the total passage approach flow and is reported as a mass flow

ratio, MFR. The leakage flow MFRs tested in the present study are 0.5%, 1.0%, and 1.5%.

**Table 2. Leakage Plenum Dimensions**

Stator Endwall Lip ( $h_s$ ):	2.14 cm
Rotor Endwall Lip ( $h_r$ ):	2.85 cm
Injection Slot ( $h_i$ ):	0.50 cm
Plenum Height ( $h_p$ ):	28.80 cm
Plenum Width ( $w_p$ ):	21.60 cm
Chamfer Angles ( $\beta$ ):	15.0°

**Figure 3. Cross-section of the leakage plenum, including endwall contours****Table 3. Cascade Freestream Approach Flow Characteristics**

Bulk Inlet Flow Properties		Turbulence Characteristics	
Inlet $Re_c$ :	430,000	$\Lambda / c$ :	0.127
$U_0$ :	11.5	$Lu / c$ :	0.190
Tu (%):	14	$\epsilon$ :	32 m <sup>2</sup> /s <sup>3</sup>

The wind tunnel flow approaching the test section has been characterized; selected quantities are given in Table 3. The approach flow is shown to have a Reynolds number (based on inlet velocity and blade chord), a turbulence level, and turbulence length scales that are representative of engine conditions. The static pressure profile is given in Fig. 4 for the upper passage where measurements are taken. It is representative of a typical mid-sized engine first stage rotor. Pressures are scaled as a pressure coefficient,  $C_p$ , as defined in Equation 1 with a measurement uncertainty of 2.5%. The major contribution to the measurement uncertainty is the precision error of an inclined manometer.

$$C_p = \frac{P_s - P_{s,0}}{\frac{1}{2}\rho U_o^2} = \frac{P_s - P_{s,0}}{P_{t,0} - P_{s,0}} \quad (1)$$

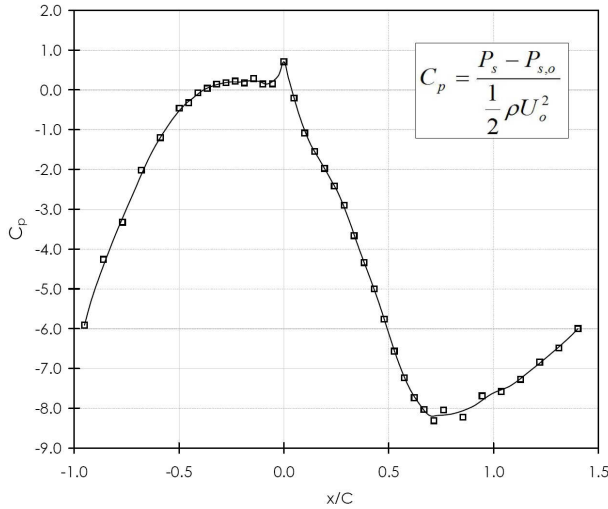


Figure 4. Blade Midspan Static Pressure Profile

## MEASUREMENT TECHNIQUES

Temperature measurements are made within the flow field and on the endwall surface to trace the leakage flow path and document mixing within the passage. This information is useful in understanding the leakage flow's cooling utility, endwall contouring effects, and endwall secondary flow behavior.

Before each experiment begins, a test section warm-up period of about 2 hours is applied to attain steady state. During this time, a resistance heater delivers energy to the auxiliary leakage flow at a rate of approximately 750 Watts. This produces an increase in leakage flow temperature of 8-10°C above the approach flow temperature (varies with flow rate). The main flow is at room temperature, typically in the vicinity of 24°C. During each experiment, temperatures are measured using seven Type-E thermocouples. Five of the thermocouples are used to measure fluid temperature at the rim seal gap. They are averaged to obtain the leakage flow temperature,  $T_\ell$ . This definition is important as in some cases mainstream fluid can flow into the leakage plenum, changing the fluid temperature delivered at the leakage flow slot. The approach flow temperature,  $T_0$ , is recorded with a single thermocouple placed slightly upstream of the inlet plane ( $x/C_{ax} = 0$ ) at mid-span and mid-pitch. Signal acquisition is handled using an Agilent 34970A unit. Both the data acquisition hardware and a three-axis motor traversing system are controlled using an in-house software program. All thermocouples are sampled at a rate of one Hz for twenty seconds for each measurement location. The samples are then time-averaged.

Flow field temperatures are measured using a thermocouple with a mild bend to allow the near-tip region to be aligned with

the flow. This probe is mounted onto a motor traversing system for movement within the blade passage. Temperatures are scaled in the form of dimensionless recovery temperatures,  $\theta$ , as shown in Eq. 2. Since the flow is of low velocity, thus kinetic energy has little effect making static and recovery temperatures essentially equal. The local variable  $T(x, y, z)$  is measured at 837 locations within the passage for each experiment. These measurements are made along selected endwall-normal planes as displayed in Fig. 5 at several streamwise locations,  $x/C_{ax}$  (-0.296, 0, 0.247, 0.44, and 0.92). As shown, measurements are more concentrated near the contoured endwall surface (bottom wall). Since differences in temperature ( $\Delta T$ ) are measured and used in computing  $\theta$ , uncertainty values are low. Typical uncertainties in  $\theta$  range from 1% to 1.3%, depending upon leakage mass flow ratio. The major contribution to uncertainty in temperature difference measurement is due to a small amount of drift in passage flow temperature during the measurement period.

$$\theta(x, y, z) = \frac{T(x, y, z) - T_0}{T_\ell - T_0} \quad (2)$$

Adiabatic film cooling effectiveness measurements are made on the endwall surface. To calculate this quantity, one must be able to accurately measure the endwall surface temperature, as well as verify that the adiabatic boundary condition ( $dT/dz|_{z=0}$ ) is satisfied there. In this study, the endwall is made of a low thermal conductivity material (0.12-0.15 W/mK) and the test section is heated until it attains steady-state operation. These conditions give rise to an endwall that very closely approximates an adiabatic surface. Near-wall temperature gradients are measured to verify that this is true. A total of 131 spatial locations (shown in Fig. 6) are visited on the endwall with the traversing thermocouple probe. Adiabatic film cooling effectiveness ( $\eta$ ) is defined in Eq. 3, showing its relation to  $\theta$ . Uncertainties in  $\eta$  are identical to those in  $\theta$  (1% to 1.3%).

$$\eta(x, y) = \theta(x, y)|_{z=0} = \frac{T(x, y)_{z=0} - T_0}{T_\ell - T_0} \quad (3)$$

## RESULTS AND DISCUSSION

Measurements made within the test section include passage thermal field maps and endwall adiabatic effectiveness contours. Each measurement was made separately with either endwall *A* or *B* geometry in place and for three disc cavity leakage mass flow ratios. These six different cases for each measurement type allow sufficient documentation of endwall contouring and leakage flow rate effects.

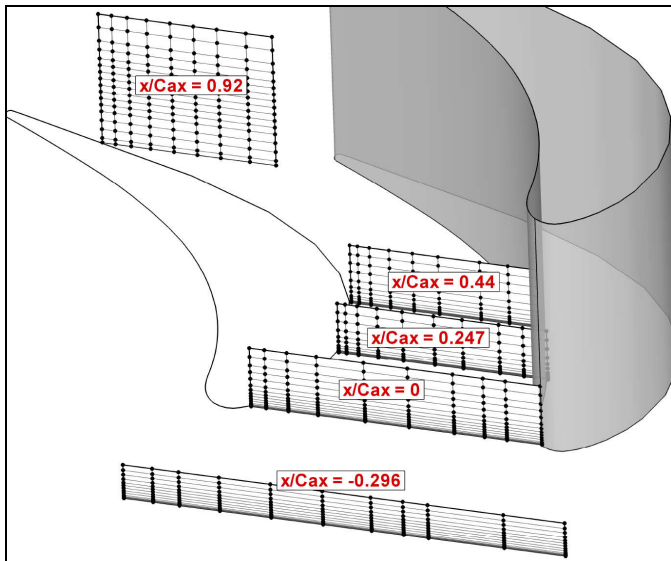


**Figure 5. Flow Field Temperature Measurement Locations**

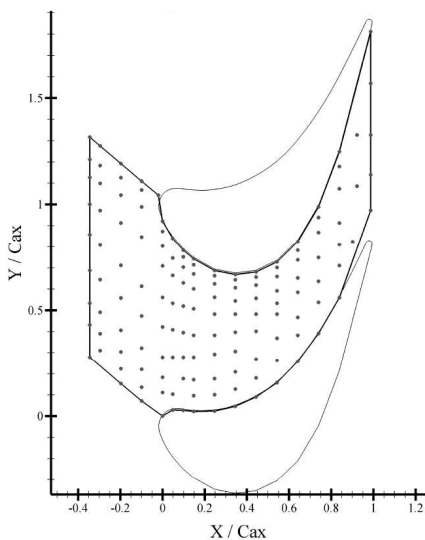


**Figure 6. Endwall Adiabatic Film Cooling Effectiveness Measurement Locations**

### Passage Thermal Fields

Results for passage temperature fields with endwall *A* geometry are shown in Figure 7. All three plots exhibit similar features. The most upstream plane ( $x/C_{ax} = -0.296$ ) displays a maldistribution in temperature for all cases. The highest temperatures are seen at the left side of this plane and steadily decrease moving rightward. The maldistribution reduces as the leakage flow rate is increased. The occurrence of lower temperatures near the leakage slot suggests that mainstream fluid may be entering the leakage plenum and mixing with the leakage flow before departing back into the passage. Additionally, the pressure field near the stagnation region of the right blade appears to be skewing the leakage flow towards the

suction side of the passage even at this upstream location. These two discussion points possibly explain why the leakage slot experiences this maldistribution.

Another similarity in the three data sets is the path and measured profile shape of the leakage fluid as it is traced through the passage. Changing the leakage flow rate in the range of 0.5-1.5% MFR appears to have no major effect on the fluid mechanics and thus coolant position within passage. With all three flow rates, the leakage fluid is quickly swept across the endwall and upwards onto the suction side of the passage. These observations suggest that the momentum of the leakage flow exiting the slot is simply too small to compete with the cross-stream passage gradient in the endwall region. As the fluid is swept across the endwall, it mixes with the passage flow due to vorticity in the passage (See ref. [9] for a description of endwall secondary flows) while still providing cooling coverage. The coverage magnitude is dependent on the leakage flow rate. A higher flow rate provides an increase in endwall cooling coverage magnitude just by virtue of having more cooling fluid delivered. This is seen as a gradual increase in dimensionless temperature values,  $\theta$ , on all planes with increasing leakage MFR rates, 0.5%-1.5%.

At a location just slightly downstream of the  $x/C_{ax} = 0.44$  plane, the leakage flow completely lifts off of the endwall surface providing cooling value only on the blade suction side surface. This “lifting” action is apparent as far upstream as the  $x/C_{ax} = 0.44$  plane -- the location of highest temperature begins to rise off the endwall. At the final passage measurement plane ( $x/C_{ax} = 0.92$ ), dispersion due to the mainstream turbulence level and passage vortices has caused much of the leakage flow to mix out, leaving very low concentrations. The maximum coverage at this location lies on the blade suction surface at approximately 30% span. This corresponds quite well with the exit plane pressure loss measurements for the same geometry, as reported in [10]. It can be concluded from the two types of measurements that this is the location to which the passage vortices has carried the entrained leakage flow.

Results for passage temperature fields with the endwall *B* geometry are shown in Figure 8 for leakage mass flow ratios of 0.5%, 1.0%, and 1.5%. Many of the flow features exhibited in these data are similar to those with the endwall *A* geometry. Again present is a temperature maldistribution at the leakage flow slot ( $x/C_{ax} = -0.296$ ). As the leakage flow rate is increased, the distribution at this slot improves; although a uniform distribution is never achieved. The leading edge plane ( $x/C_{ax} = 0$ ) for the endwall *B* data is at a lower elevation than that of endwall *A*. This is due to the difference in surface contours. The maximum temperature at this plane occurs at approximately  $y/C_{ax} = 0.56$  for the case of leakage MFR=0.5%. As the leakage flow rate is increased, the area of maximum  $\theta$  extends horizontally over the endwall surface. As this area of high  $\theta$  extends, it favors the suction side of the passage. One observation of importance is that the area of

highest  $\theta$  appears to be slightly elevated off the endwall surface for all three leakage flow rates cases. This results in decreased cooling coverage of the endwall by the leakage fluid.

At the measurement plane  $x/C_{ax} = 0.247$  leakage fluid is migrating toward the passage suction side and is diminishing in  $\theta$  value. At this passage location, the  $\theta$  maximum is very near the corner formed by the blade and endwall. Slightly downstream,  $x/C_{ax} = 0.44$ , the area of maximum  $\theta$  appears to begin moving up the blade's suction side surface. This movement leaves very little endwall cooling coverage at the  $x/C_{ax} = 0.44$  plane. The final measurement plane at  $x/C_{ax} = 0.92$  reveals that most of the leakage fluid has been mixed out to a point where it cannot be detected. This is the case with the lowest leakage flow rate. As the leakage flow rate is increased, some leakage fluid may be identified at this plane. The fluid appears to have mixed out within the passage and exists in a horizontal band between 10-30% span.

A comparison of the passage thermal field follows: The first finding is independent of endwall contouring considerations and relates to the leakage flow slot temperature distribution and the possibility of mainstream flow ingression. It was initially found that lower  $\theta$  fluid was being delivered through the leakage cavity slot near the center blade stagnation region than at other locations along the slot. Monitoring the temperatures at several locations within the leakage plenum, as well as reviewing the passage temperature field data sets revealed this trend for all leakage flow cases. Since a fairly uniform temperature is being injected into the leakage plenum along the rim seal slot (as monitored by measurements), the only reason a drop in  $\theta$  should occur within the plenum is due to mainstream flow ingression. The driving force behind the suspected ingression is possibly the presence of the downstream blade and its effects on the local static pressure field. This is not evident at the same relative location near the upper blade, indicating a less than ideal periodicity from one passage to the next. This is the product of having only two passages and having a flow delivery passage that is so sensitive to downstream conditions. Because of this, a study of the film cooling coverage upstream of the center blade leading edge is more reliable than a study of the values upstream of the upper blade leading edge.

Another important observation which is contour dependent relates to endwall cooling coverage provided by the leakage fluid. It appears that for the endwall *B* cases, leakage fluid is slightly displaced away from the endwall surface at the leading edge plane. By displacing the leakage flow away from the endwall surface, its utility as a coolant is significantly diminished. This "leakage flow displacement" behavior is not visible in any of the endwall *A* results. The cause for this discrepancy is unknown; however, it is speculated to be due to the surface contour itself. Endwall *A* incorporates strong curvature, thus an acceleration profile. The endwall *B* curvature, however, should lead to a relatively weaker acceleration. Thus its boundary layer is thicker than its counterpart due to the

lesser acceleration, thus it displaced the leakage flow away from the endwall surface more. If the cause of this discrepancy is indeed geometry dependent, it suggests that the endwall *A* contour is superior with respect to heat transfer considerations on the endwall.

Another noticeable difference between the data sets for the two endwall shapes is in the temperature magnitudes. Endwall *A*'s data appear to have higher peak temperatures on planes  $x/C_{ax} = 0.247$ ,  $0.44$ , and  $0.92$ . This reveals that in the endwall *B* geometry, the leakage flow is mixed out faster, thus diminishing the  $\theta$  values. In general, however, temperature profiles on these measurement planes do not differ significantly in either shape or size. This suggests that dispersion of the leakage flow is little affected by endwall shape.

### **Endwall Adiabatic Effectiveness**

Endwall adiabatic effectiveness results are reported in Figure 9 for the endwall *A* geometry with leakage mass flow ratios of 0.5, 1.0, and 1.5%. In analyzing the three data sets, one sees the improved cooling coverage provided by increasing the leakage flow rate. That is, effectiveness magnitudes increase as leakage flow rate increases, though the cooling "pattern" does not differ strongly. Another general observation is that near-zero effectiveness values exist within the passage beyond the streamwise position of  $x/C_{ax} = 0.6$ . This finding reveals that all of the leakage flow has been removed from the endwall by mechanisms likely related to endwall secondary flows (i.e. passage vortex entrainment and cross-stream pressure gradient) regardless of leakage flow rate. The effect of cross-stream pressure gradient is also quite apparent upstream of the leading edge plane as leakage flow is skewed toward the passage suction side. These general observations are expected and agree with results of many other studies on the topic [e.g. Pau et al. 2008].

Additionally, in all three data sets, a local peak in endwall adiabatic effectiveness occurs at approximately  $x/C_{ax} = 0$  and  $y/C_{ax} = 0.6$ . This rise in effectiveness is quite apparent in reviewing the contour plots as it stands out within the surrounding data which, in general, decreases with streamwise distance. This region of increased effectiveness appears to be dependent on leakage flow rate as the peak-to-trough difference becomes larger when the flow rate is increased from 0.5% to 1.5% MFR. The dependence of this feature on endwall contouring cannot be established from these data sets alone as they share the same endwall geometry. The fact that it increases with leakage flow rate does, however, suggest that it may depend on boundary layer thickness, acceleration, or impingement upon the airfoil leading edge. Further comparisons with the endwall *B* geometry will provide more information on differences caused by contouring.

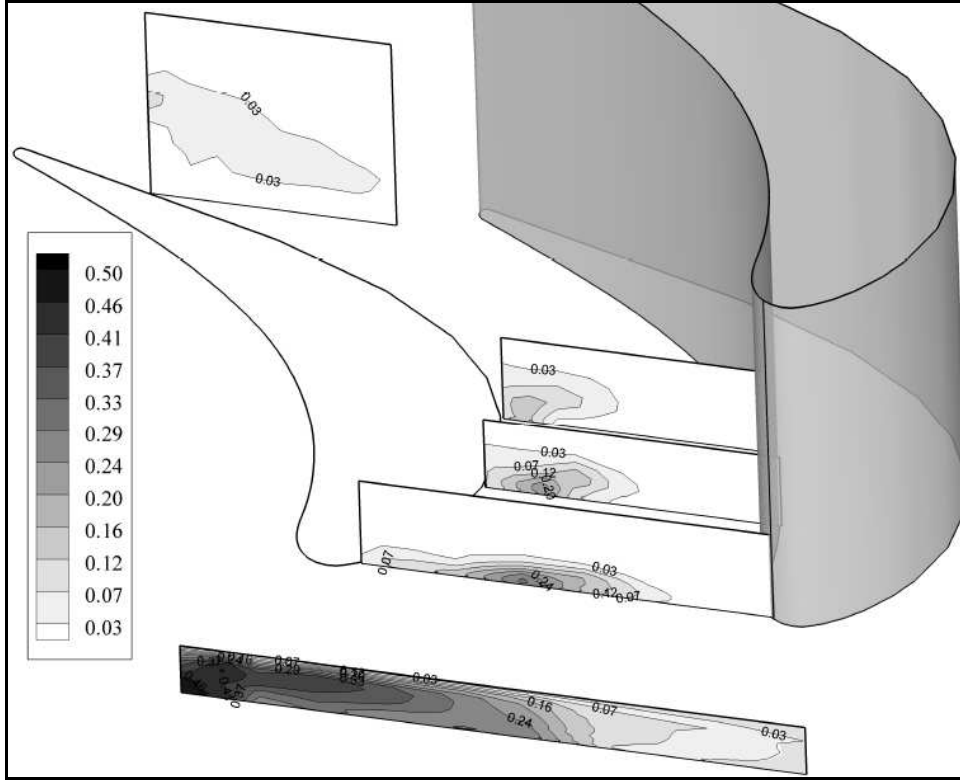


Figure 7a. Passage Thermal Field Maps for Endwall A with Leakage MFR of 0.5%

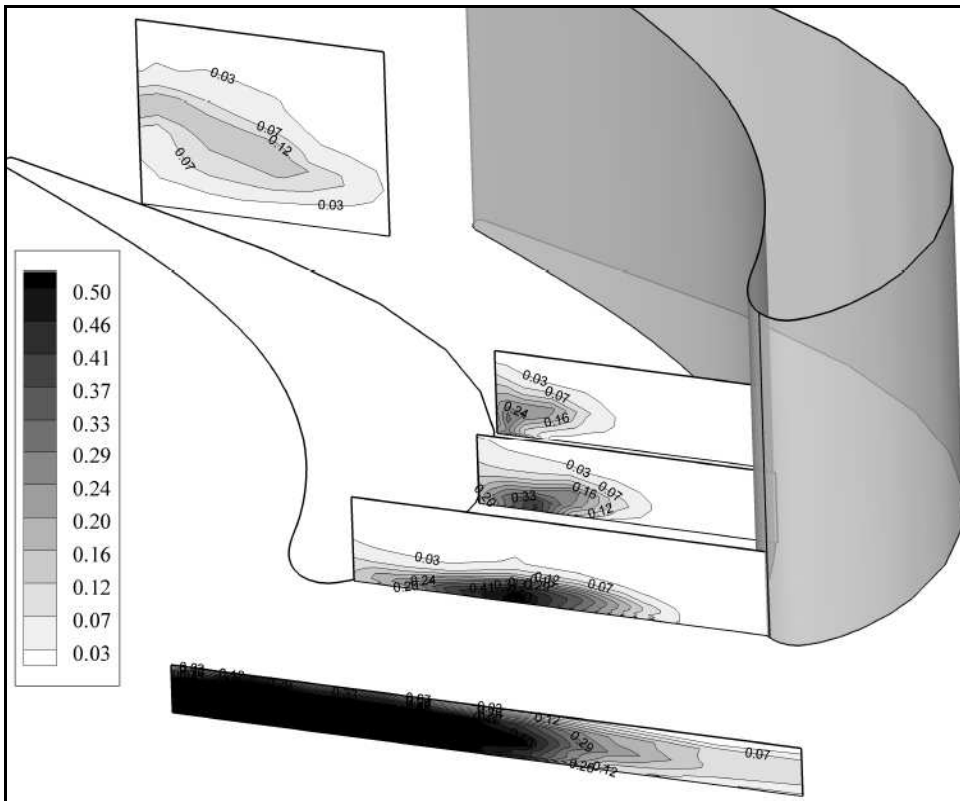


Figure 7b. Passage Thermal Field Maps for Endwall A with Leakage MFR of 1.0%

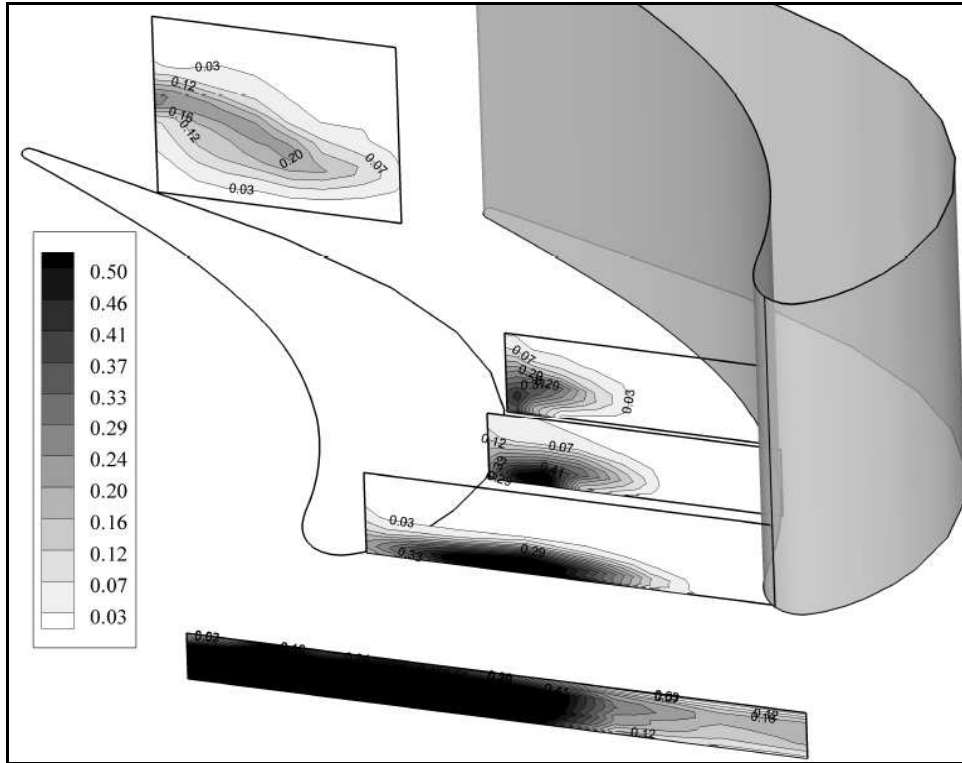


Figure 7c. Passage Thermal Field Maps for Endwall A with Leakage MFR of 1.5%

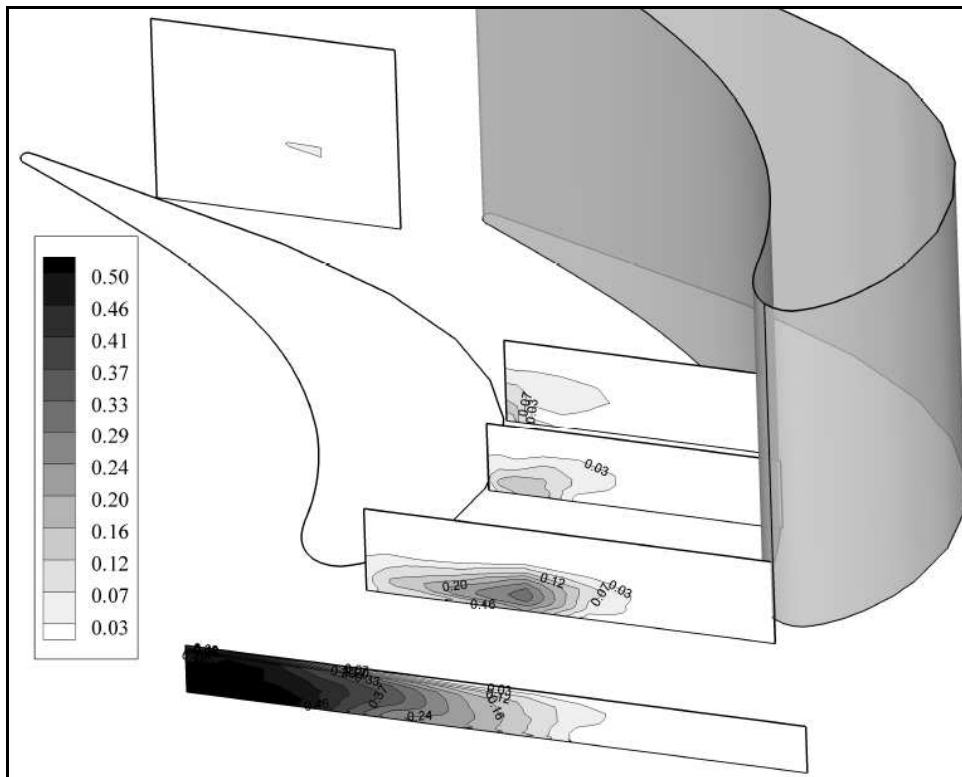


Figure 8a. Passage Thermal Field Maps for Endwall B with Leakage MFR of 0.5%

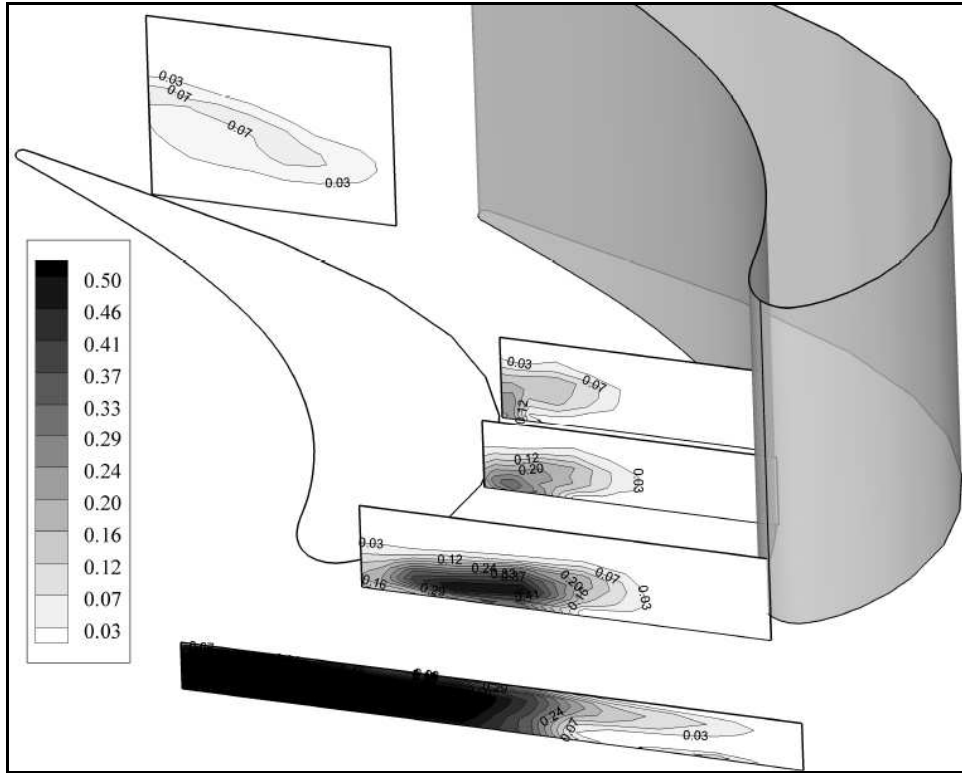


Figure 8b. Passage Thermal Field Maps for Endwall *B* with Leakage MFR of 1.0%

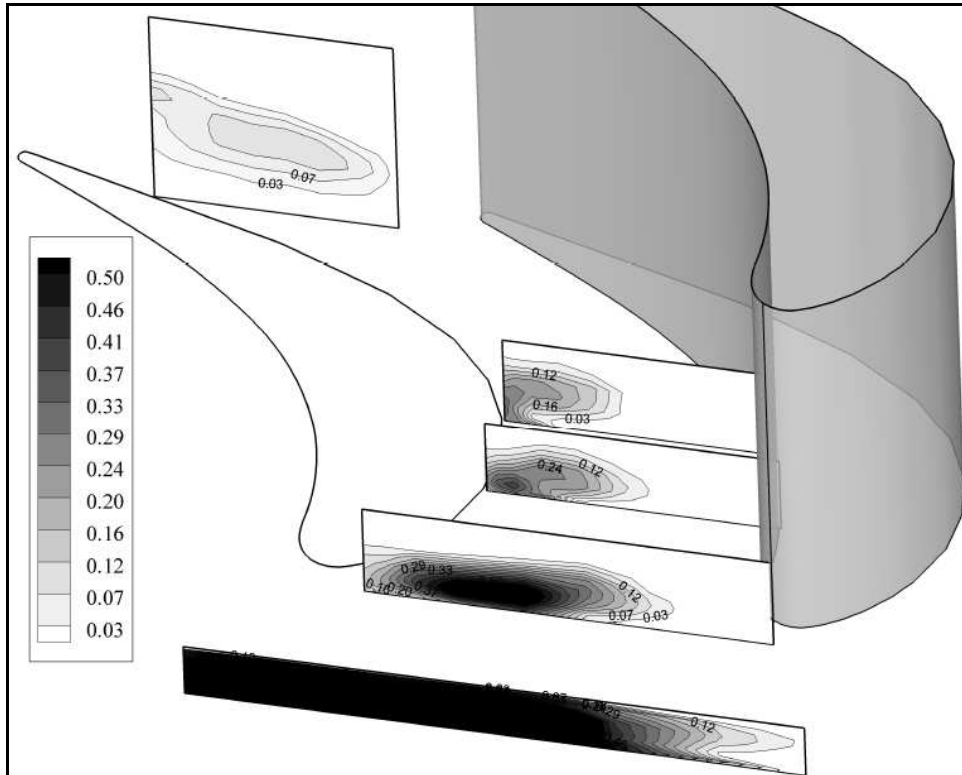
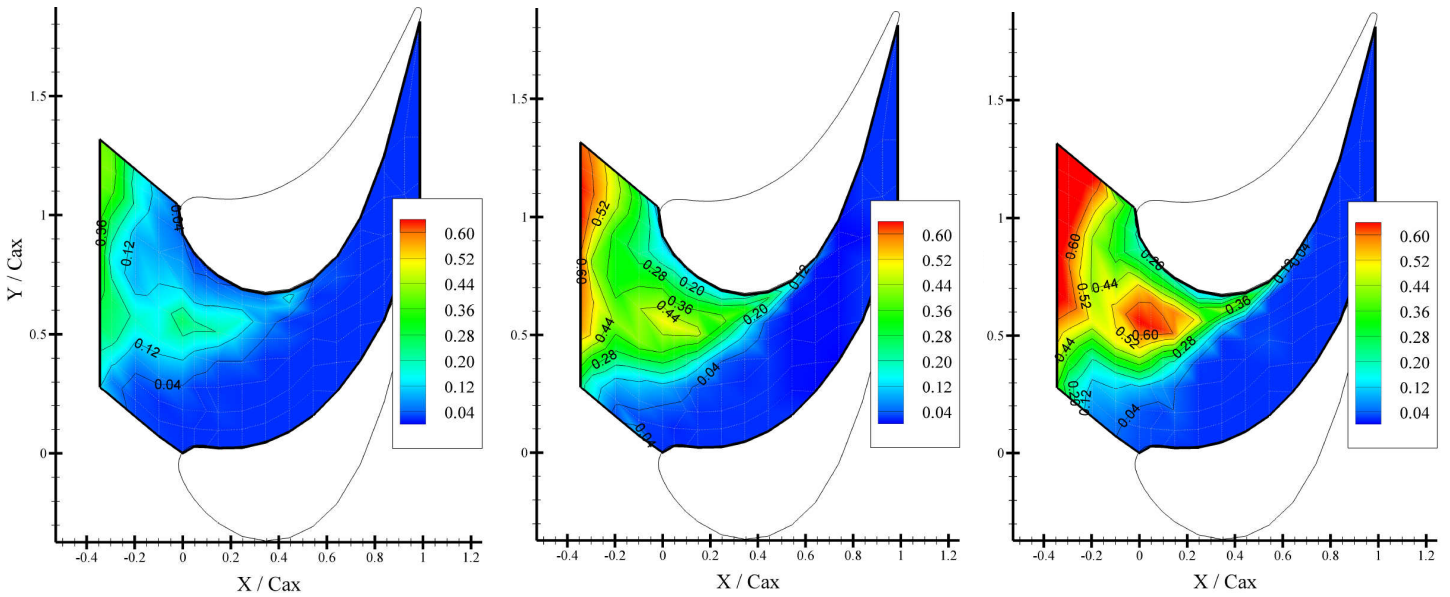
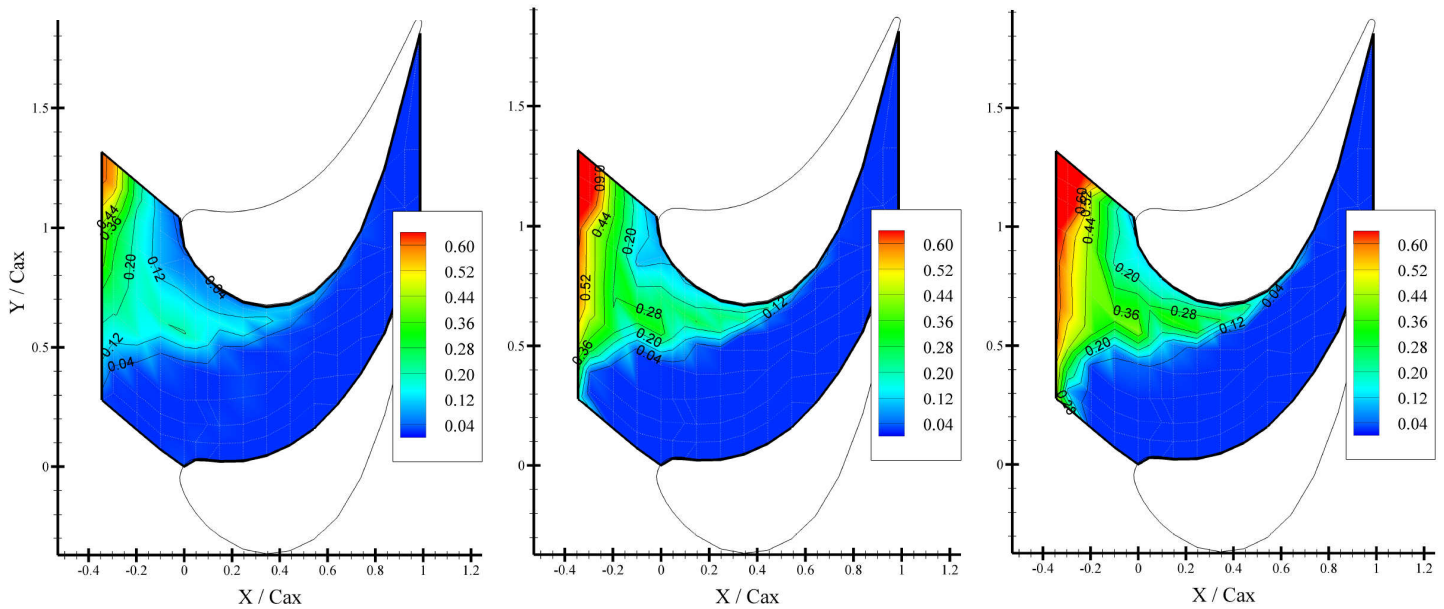


Figure 8c. Passage Thermal Field Maps for Endwall *B* with Leakage MFR of 1.5%



**Figure 9. Endwall Adiabatic Film Cooling Effectiveness Contours for Endwall A with Leakage MFR of 0.5% (Left), 1.0% (Center), and 1.5% (Right)**



**Figure 10. Endwall Adiabatic Film Cooling Effectiveness Contours for Endwall B with Leakage MFR of 0.5% (Left), 1.0% (Center), and 1.5% (Right)**

A third observation, valid for all three leakage MFR's is the lower cooling coverage near the blade suction side-to-endwall corner in the first half of the passage. This is seen as lower effectiveness values from the airfoil leading edge and downstream in the airfoil-to-endwall corner. The feature is difficult to see in the 0.5% MFR case as there is little cooling coverage in neighboring areas. One plausible explanation for the ineffective cooling coverage in this region for all three flow rates is that the suction-side leg of a horseshoe vortex is preventing leakage flow from entering this area. At some

downstream location, the horseshoe vortex and endwall boundary layer flow tend to rise off the endwall, in which case leakage flow would be able to reach the corner. This may be, since the effectiveness does increase in the suction side-to-endwall corner further downstream, at approximately  $x/C_{ax} = 0.4$ .

Equivalent cases with the endwall B geometry are reported in Figure 10. In general, there is an improvement seen in effectiveness magnitude as the leakage flow increases. The affected surface area does not significantly change with leakage

flow rate. Several other observations can be made without regard to leakage flow rate. Firstly, endwall cooling effectiveness is concentrated to the suction side of the passage. Regions very close to the leakage slot provided fairly uniform coverage; however, the effectiveness patterns are quickly skewed by, most likely, the passage pressure gradient. A second observation is that the leakage flow does not provide much coverage near the upper blade's stagnation point or suction side-to-endwall corner. Performance does improve with an increased leakage MFR; however, these regions are still covered less effectively than seen in the mid-passage areas. It is worth noting that remnants of the leakage flow on the endwall entirely disappear at a downstream position of  $x/C_{ax} = 0.6$ . This corresponds well with the endwall *A* results. Also, endwall *B*'s results do not appear to exhibit any localized peaks in effectiveness magnitude, contrary to the results with endwall *A* (e.g. Figure 9 [ $x/C_{ax}=0$ ,  $y/C_{ax}=0.55$ ]). This suggests that the occurrence of these localized peaks is related to wall contouring.

#### Pitch-Averaged Endwall Adiabatic Effectiveness Data

For discussion purposes, endwall adiabatic effectiveness data are pitch-averaged and compared in Figure 11. For all measured cases, peak adiabatic effectiveness ( $\eta$ ) values are seen at the leakage slot location ( $x/C_{ax} = -0.345$ ). The fact that  $\eta$  values at the leakage slot are not equal to unity (wall temperatures not equal to those at rim seal) indicates that an undesired mixing process is taking place within the leakage plenum to decrease the adiabatic effectiveness. In this experiment, only mainstream fluid could cause this change. This finding is strong evidence that mainstream flow ingress is taking place within the test section. Furthermore, since the endwall effectiveness values are not equal to one another for the three cases, it can be said that the degree of flow ingress is dependent upon the leakage flow rate; higher leakage flow rates allowing for less ingress. The endwall contour appears to have little effect. Moving downstream of the leakage slot, one sees that a steep decrease in  $\eta$  values occurs until roughly  $x/C_{ax} = -0.2$ . These data reveal that most of the leakage flow's endwall cooling potential has been lost between the leakage slot ( $x/C_{ax} = -0.345$ ) and this location, regardless of leakage flow rate. Further downstream, endwall contouring is a dominating factor. Endwall *A* exhibits a leveling behavior as  $\eta$  values remain stable. These values are dependent upon leakage flow rate, especially for endwall *A*. One proposed explanation for this behavior is that the endwall contour is causing fluid acceleration in this area, thus locally decreasing leakage-to-mainstream mixing effects. From the leading edge plane and downstream into the passage, the pitch-averaged adiabatic effectiveness data gradually decrease in a fairly linear fashion for all leakage flow rates. At  $x/C_{ax} = 0.75$ , remnants of the leakage fluid coolant coverage have completely disappeared.

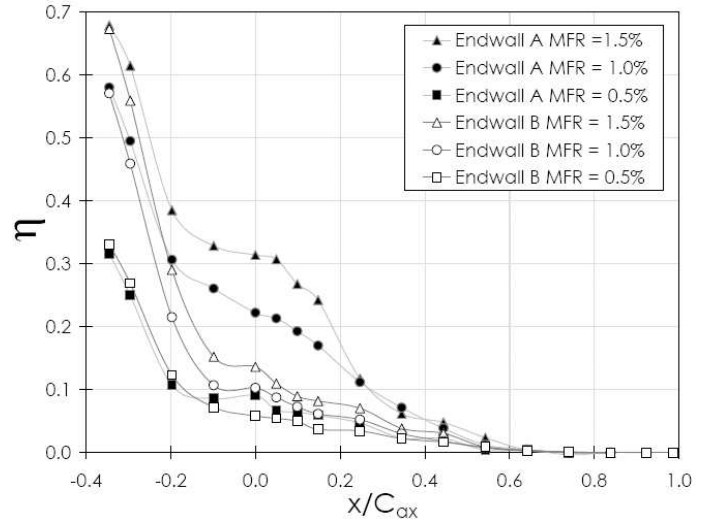


Figure 11. Pitch-Averaged Film Cooling Effectiveness Values Comparing Endwalls *A* and *B*

#### CONCLUSIONS

An experimental study of passage flow and leakage flow mixing around the hub endwall region in a linear cascade of rotor blades has been performed. The subject of endwall contouring has been investigated through the inclusion of two different endwall profiles. Leakage flow is injected from a plenum which replicates dimensions found in a disc cavity between stator and rotor blades. The leakage flow rate is metered and set at mass flow ratios of 0.5%, 1.0%, and 1.5% of the passage approach flow rate during these tests. The wind tunnel facility is operated at an engine-representative Reynolds number ( $4.3 \times 10^5$ ) with high freestream turbulence intensity (14%) and large length scales (10% of  $C$ ).

During wind tunnel operation, disc cavity flow ingress was found as evidenced by measurements of passage thermal fields. The most upstream passage thermal field map showed this occurrence as a reduction in normalized temperature,  $\theta$ , between the rim seal location and leakage slot. This finding was shown to be dependent upon leakage mass flow ratio. Increases in leakage MFR led to increases in temperatures (less flow ingress) at the leakage slot. The two endwall contours tested were found to have no significant effect on the occurrence of ingress. Additionally, flow in the region of the leakage slot was found to be highly unsteady using smoke particle and tuft flow visualization and hotwire measurements (not included herein).

A comparison of thermal performance between the endwall contours was made through endwall adiabatic effectiveness and passage thermal field results. Endwall cooling coverage patterns remained the same size and shape regardless of endwall contour. This signifies the relative strength of passage secondary flows on endwall cooling. The extent to which leakage flow provided cooling utility within the passage was limited by the passage vortex separation line. This line was

clearly seen in all endwall thermal measurements. Endwall adiabatic effectiveness patterns for both contours were roughly of the same shape and size; however, their magnitudes differed. The endwall *A* geometry consistently produced higher effectiveness magnitudes at equivalent leakage flow rates. This was corroborated and further explained by the passage temperature field measurement results. By comparing temperature fields of similar cases, it was seen that the endwall *B* geometry causes a slight displacement of leakage flow away from the endwall surface. It was seen most clearly near the leading edge plane, and occurred with all three leakage flow rates tested. The net effect was a diminished utility of leakage flow with the endwall *B* contour. This occurrence was not seen with endwall *A* as its profile caused acceleration which kept leakage flow closer to the endwall surface.

Also, the effects of variations of disc cavity leakage flow rate were documented. Thermal measurements on the endwall revealed that increasing the leakage flow rate directly increased adiabatic effectiveness values. Pitchwise-averaged effectiveness data showed also that increasing the leakage MFR from 1.0 to 1.5% produced diminishing returns when compared to an increase in effectiveness when MFR was changed from 0.5 to 1.0%. This was true irrespective of endwall contour.

#### ACKNOWLEDGMENTS

We are grateful for sponsorship of this work by Solar Turbines Inc. Also, we are grateful for resources from the University of Minnesota Supercomputing Institute.

#### REFERENCES

- 
- [1] Maclean, C., Camci, C., Glezer, B., 2001, "Mainstream Aerodynamic Effects due to Wheel-space Coolant Injection in a High-Pressure Turbine Stage: Part I – Aerodynamic Measurements in the Stationary Frame", *Journal of Turbomachinery*, Vol. 123
- [2] Dénos, R., Paniagua, G., 2002, Influence of the Hub Endwall Cavity Flow on the Time-Averaged and Time-Resolved Aero-Thermodynamics of an Axial HP Turbine Stage, ASME Turbo Expo 2002, GT2002-30185.
- [3] Paniagua, G., Dénos, R., and Almeida, S., 2004, Effect of the Hub Endwall Cavity Flow on the Flow-Field of a Transonic High-Pressure Turbine, ASME Turbo Expo 2004, GT2004-53458.
- [4] Pau, M., Paniagua, G., Delhayé, D., de la Loma, A., and Ginibre, P., 2008, Aerothermal Impact of Stator-Rim Purge Flow and Rotor-Platform Film Cooling on a Transonic Turbine Stage, ASME Turbo Expo 2008, GT2008-51295.
- [5] Ong, J.H.P., Miller, R.J. and Uchida, S., 2006, "The Effect of Coolant Injection on the Endwall Flow of a High Pressure Turbine," ASME Turbo Expo 2006, GT2006-91060.
- [6] Marini, R., and Girgis, S., 2007, The Effect of Blade Leading Edge Platform Shape on Upstream Disk Cavity to Mainstream Flow Interaction of a High-Pressure Turbine Stage, ASME Turbo Expo 2007, GT2007-27429.
- [7] Blair, M.F., 1974, "An Experimental Study of Heat Transfer and Film Cooling on Large-Scale Turbine Endwalls," ASME J. of Heat Transfer, 96, pp. 524-529.
- [8] Biesinger, T.E., Gregory-Smith, D.G., 1993, "Reduction of Secondary Flows and Losses in a Turbine Cascade by Upstream Boundary Layer Blowing," ASME Turbo Expo 1993, 93-GT-114.
- [9] Simon, T.W., and Piggush, J.D., 2006, Turbine Endwall Aerodynamics and Heat Transfer, *J. of Propulsion and Power*, Vol. 22, No. 2, pp. 301-312.
- [10] Erickson, R. and Simon, T.W., 2009, "Effects of Stator/Rotor Leakage Flow and Axisymmetric Contouring on Endwall Adiabatic Effectiveness and Aerodynamic Loss," ICHMT Turbine 09, International Symposium on Heat Transfer in Gas Turbine Systems, Antalya, Turkey.
- [11] Suryanarayanan, A., Mhetras, S.P., Schobeiri, M.T., and Han, J.C., 2006, "Film Cooling Effectiveness on a Rotating Blade Platform," ASME Turbo Expo 2006, GT2006-90034.